Effectiveness of Large-Camber Circular Arc Airfoil at Very Low Reynolds Numbers*

Masato OKAMOTO[†] and Keita EBINA

Department of Aeronautics, Kanazawa Institute of Technology, Nonoichi, Ishikawa 921–8501, Japan

The objective of this study is to ascertain the steady-state aerodynamic characteristics of a thin circular arc airfoil with a large-camber by comparing its camber with various cambers at Reynolds numbers ranging from 1×10^3 to 10×10^3, similar to that of insect flight. A large camber of over 20% chord is seen in the elytra of beetles (*Coleoptera*), many of which fly by opening the elytra. A low-pressure wind tunnel that we uniquely designed was used to measure the very small forces and moment acting on the wing. As a result, a high maximum lift coefficient was obtained for a large-camber circular arc airfoil, even at Reynolds numbers less than 3×10^3. In addition, the pitching moment of the airfoil was found to be zero in a wide range of angles of attack when the moment center was set to the appropriate position. The large-camber circular arc airfoil will be useful in designing very-low Reynolds number aircraft such as insect-sized micro-air vehicles (MAVs).

Key Words: Aerodynamic Characteristics, Airfoil, Low Reynolds Number, Wind Tunnel Testing

1. Introduction

Thin circular arc airfoils and thin airfoils with angular profiles such as corrugated airfoils that are seen in the sections of insect wings show good performance at Reynolds numbers of $Re \leq 1 \times 10^4$, similar to insect flight. Two-dimensional aerodynamic characteristics of thin airfoils at $Re \leq 1 \times 10^4$ have been investigated by measuring the aerodynamic forces acting on a wing by Okamoto et al.,[1] Azuma et al.,[2] Kesel,[3] and Sunada et al.[4] The aerodynamic characteristics in a wide range of angles of attack of more than 90 deg were investigated by Zhou et al.[5] and those of three-dimensional wings were investigated by Okamoto and Azuma.[6] The flow around a corrugated profile has been investigated by Obata and Shinohara[7] and Shi et al.[8] In addition, computational solutions of the flow around an airfoil and the forces acting on a wing were simulated by Kunz and Kroo,[9] Vargas et al.,[10] Levy and Seifert,[11] Kim et al.[12] and Hord and Lian.[13]

Recently, we investigated the aerodynamic characteristics of thin airfoils having cambers from 3%c to 9%c for a Mars exploratory airplane (which performs in very low Reynolds number flows because of the very small atmospheric density on Mars) by measuring the lift, drag and pitching moment acting on the wing in a low-speed wind tunnel at $3 \times 10^3 \leq Re \leq 20 \times 10^3$.[14] In this study, cambers between 3%c and 6%c were confirmed to show the largest lift-to-drag ratio at $Re \leq 10 \times 10^3$. However, the impact of a change in camber on the lift-to-drag ratio was found to decrease as the Reynolds number decreased. The effects of variations in Reynolds number on the selection of the camber for an insect-sized thin airfoil are largely unknown. For the purpose of the present study, in addition to these results, we consider the assumption that airfoils with a large camber over 20%c, whose application is mostly limited to airplane wing flaps, may be useful for insect-sized wings. We base this assumption on the observed presence of a similar large-camber thin airfoil in the elytra sections of beetles, many of which fly by opening these elytra.[15–17] The objective of the present study is to ascertain the steady-state aerodynamic characteristics of a thin circular arc airfoil having a large camber by comparing its performance with airfoils of various other cambers through wind tunnel tests conducted at $1 \times 10^3 \leq Re \leq 10 \times 10^3$, which correspond to insect flight.

There was a limit to the accuracy of the aerodynamic forces and moment acting on the wing measured in a low-speed wind tunnel at $Re \leq 3 \times 10^3$, even when using the sensitive balance that we developed. In order to overcome this difficulty, we designed a unique low-pressure wind tunnel for use in the present study. The low-pressure wind tunnel is effective for investigating low Reynolds number wings. For example, Anyoji et al.[18,19] investigated the airfoil used for a Mars exploratory airplane.

The two-dimensional aerodynamic characteristics of the thin circular arc airfoils were measured in this wind tunnel using rectangular wing models. In addition, although industrial applications of the airfoil were not considered in the present study, the elytra of the Japanese cockchafer (*Coleoptera*) were tested to ascertain the aerodynamic characteristics of a three-dimensional wing having a large-camber airfoil. We found that the aerodynamic characteristics of a thin circular arc airfoil having a camber of over 20%c are effective not only for aerodynamic forces, but also the pitching moment at $Re \leq 3 \times 10^3$. These experimental results will be useful in designing low Reynolds number aircraft such as micro-air vehicles (MAVs and especially, small MAVs). For example, an insect-sized MAV was proposed by Wood et al.[20] and Kroo and Kunz.[21]

We have presented a similar experimental study regarding the flight of a beetle[17] prior to this study. However, the present study, in which the aerodynamic characteristics of the thin circular arc airfoils were tested in detail, is an extension of our previous study.

2. Experimental Materials and Methods

A low-pressure wind tunnel was used to measure the very small forces and moment acting on a small wing in very low Reynolds number flows, as shown in Fig. 1. The very small wind tunnel installed in a low-pressure chamber (vacuum desiccator, Shin-ei Sangyou Co., Ltd.) made of acrylic plate is a pusher-type wind tunnel with a rectangular test section 160 mm (H) × 100 mm (W) and 180 mm in length. To reduce the length of the wind tunnel, wind flow is provided by six small direct-current fans (Sanyo Denki Co., Ltd., 9GV1212P1J01) installed upstream of the chamber, which consists of a straightening honey comb and six sheets of 40 mesh nylon screens. The contraction ratio between the area of the settling chamber and the area of the test section is 9. The wind velocity U at the test section is regulated from 2 to 5 m/s in each low-pressure environment between 0.1 atm and 1 atm (atmospheric pressure) by changing the rotational speed of the fans driven by the PWM system. The turbulence intensity along the wind velocity was less than 0.3% ($\sqrt{\overline{u}}/U < 0.3\%$) at 1 atm. The wind velocity U was determined by a Pitot tube, and the very small differential pressure between the total and static pressures was measured using an electric manometer (Okano Works, Ltd., DMP200N). By analyzing the Strouhal number, which is a function of the Reynolds number based on the diameter of a circular cylinder,[22] the correction coefficient of the Pitot tube was confirmed by counting the frequency of the Karman vortex street observed downstream of the circular cylinder using a hotwire anemometer. The aerodynamic coefficients of the lift, drag and pitching moment of a thin flat plate obtained at each Reynolds number correspond to the results measured at the same Reynolds number in another environment of different atmospheric pressure.

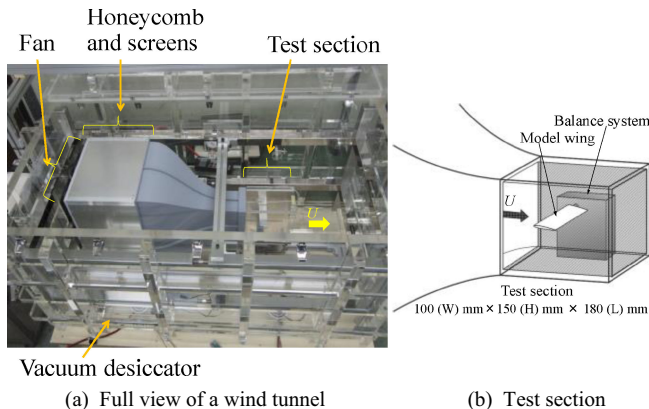The load measuring device was made by the authors from some aluminum blocks, onto which the strain gauges were attached, and the lift l, drag d and pitching moment about 25%c $m_{0.25c}$ were measured. To vary the angle of attack, the wing model was rotated by the driving mechanism of a stepping motor controlled by a microcomputer. The output signals of the measuring device were analyzed using a personal computer through a bridge circuit, strain amplifier and 16-bit analog-to-digital converter. The aerodynamic data at various angles of attack α were obtained by averaging 300 datasets measured at a sampling frequency of 100 Hz. An averaging time of 3 s produced sufficiently high repeatability of the output data. The minimum readable values were 3.4×10^{-5} N for the lift, 2.2×10^{-5} N for the drag and 2.1×10^{-7} Nm for the pitching moment. The output signals of the load cells were highly linear in the measurement range.

The non-dimensional aerodynamic coefficients of the wing, which are the lift coefficient C_l, drag coefficient C_d and pitching moment coefficient C_m, are given by the following equation by normalizing with the model wing area S for forces and Sc for moment:

$$C_l = 2l/\rho U^2 S, \quad C_d = 2d/\rho U^2 S, \quad C_m = 2m/\rho U^2 Sc \quad (1)$$

where, the wing area S is the chord c for the two-dimensional wing in the pressure measurement, as stated later.

For a three-dimensional wing, chord c is the mean aerodynamic chord $\bar{c}$, which is given by the following equation:

$$\bar{c} = \frac{2}{S} \int_0^{b/2} c^2 \mathrm{d}y \quad (2)$$

To obtain the aerodynamic characteristics of the two-dimensional wing, the wing model attached to the measuring device was placed between two side walls of the test section, as shown in Fig. 1(b). The clearance between the wing tip and the wall is less than 2% of the chord. Although this clearance was slightly large compared to that shown by Mueller,[23] we confirmed the effect of this clearance on the measurements to be negligible using the typical wing model in this study. It was subsequently confirmed, using a hotwire anemometer, that the distribution of the flow velocity between the two walls in the test section is constant except in the range of 3 mm near the surface of the wall, which is equivalent to 94% of the wing width of the models. Further, the actual wings of the elytron were set away from the walls in the test section to obtain the three-dimensional characteristics.

Figure 2 shows the airfoils used in this study: a thin flat plate with a thickness of 1.7% chord and thin circular arc airfoils made from a thin aluminum plate with a thickness of 1% chord. The cambers were varied from $h = 3\%c$ to $h = 21\%c$; these airfoils are referred to as $h\%$ circular arc airfoils in this
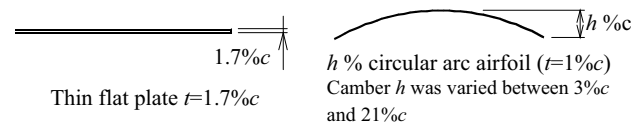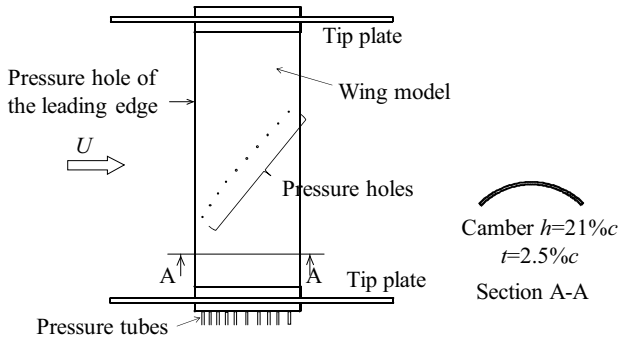

Honeycomb
Fan   and screens   Test section

Balance system
Model wing

U

Test section
100 (W) mm × 150 (H) mm × 180 (L) mm

Vacuum desiccator

(a) Full view of a wind tunnel   (b) Test section

Fig. 1.   Low-pressure wind tunnel used in this study.

1.7%c

Thin flat plate t=1.7%c

h %c

h % circular arc airfoil (t=1%c)
Camber h was varied between 3%c
and 21%c

Fig. 2.   Airfoils tested in this study.

Fig. 3. Wing model for the pressure distribution measurement.

Fig. 4. Aerodynamic characteristics of the thin flat plate.

paper. The sections of the leading- and trailing-edges of all wing models were slightly thicker as the result of cutting them vertically. The wing models are rectangular in planform, with an aspect ratio of 3.3 and a chord length of 30 mm. These wing models were examined by varying the Reynolds number between 1×10^3 and 10×10^3. Further, by comparing the aerodynamic coefficients of a wing having a similar short chord with a small blockage effect, it was confirmed that the blockage effect of the wing model, set in the test section, was negligible for the tested range of angles of attack.

The low-pressure wind tunnel is inadequate for experiments such as those for visualizing the flow around an airfoil because the test section of the wind tunnel set in a sealed vessel is too small. The two types of wind tunnels compared during the development of the present low-pressure wind tunnel to confirm wind tunnel performance were used for flow visualizations and determining the pressure distributions on the airfoil. The flows in these test sections have the same level of turbulence intensity.

Flow visualization around the airfoil was conducted using a two-dimensional smoke wind tunnel and the smoke-wire method. The streak lines were recorded using a high-speed movie camera at a frame rate of 60 frame/s.

The pressure distributions on the wing were measured using the model wing installed in another small pusher-type wind tunnel. For better delineation of this wind tunnel, please refer to Okamoto and Azuma.[6] Figure 3 shows the model wing with 0.5 mm diameter pressure holes. The thickness of this model wing is 2.5%c, which is larger than that of the wing model used in the force measurements. The pressures were measured using an electric manometer. The minimum readable pressure was 0.01 Pa and the response time was 1.0 s. The mean pressures of the output data of 5 s were used in this study.

3. Results and Discussion

3.1. Aerodynamic characteristics of the airfoils tested

Figures 4–7 show the aerodynamic characteristics of the thin flat plate and the thin circular arc airfoils with cambers of 3%c, 12%c and 21%c, which have distinctive aerodynamic characteristics by the camber, measured at Reynolds numbers ranging from 1×10^3 to 10×10^3.
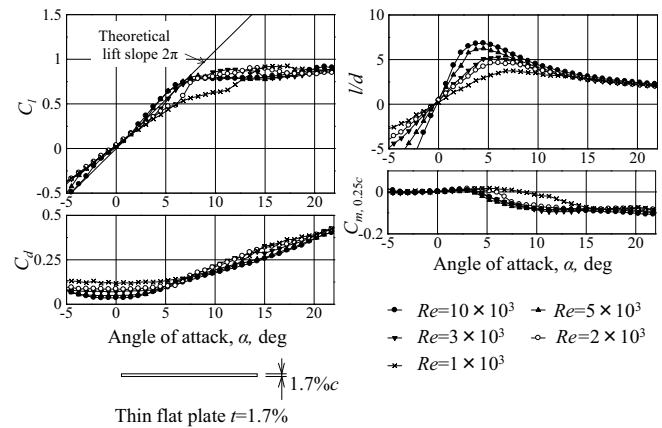
3.1.1. Thin flat plate

Figure 4 shows the aerodynamic characteristics of the thin flat plate with thickness 1.7%. As shown in the lift curve at $Re = 10 \times 10^3$, the lift coefficient C_l increases proportionally with the increase of angle of attack α, and remains constant at $\alpha \geq 7$ deg. The effect of the Reynolds number for a thin flat plate is comparatively small, because the lift curves are close to the experimental C_l measured by Mueller[23] at $Re = 80 \times 10^3$. However, the nonlinearity of the lift curve is quite remarkable as the Reynolds number decreases to 10×10^3 or less. The lift slope at $\alpha < 3$ deg is slightly smaller and the lift slope at $\alpha > 3$ deg exceeds the theoretical value of the two-dimensional lift slope of 2π at $Re = 10 \times 10^3$. This is due to the vortex lift of the separation bubble generated at the leading-edge. As the angle of attack increases, the location of the reattachment moves to the rear, as described by Crompton and Barrett.[24] As the Reynolds number decreases to 3×10^3 or less, the lift slope at $\alpha > 3$ deg temporarily decreases, and the angle of attack where the lift slope increases over 2π increases to 7 deg at $Re = 2 \times 10^3$ and to 12 deg at $Re = 1 \times 10^3$.

The drag coefficient C_d increases according to the increase of C_l. As the Reynolds number decreases, C_d increases as the minimum drag coefficient increases, which is slightly larger than twice the skin friction drag $2C_f$, as shown in Fig. 4. The increase in C_d causes the lift-to-drag ratio l/d to decrease.

The pitching moment coefficient about 25%c $C_{m,0.25c}$ has a slightly positive slope at -3 deg $< \alpha < 3$ deg, and the slope of $C_{m,0.25c}$ changes gradually to negative as the angle of attack increases. Although an additional vortex lift by the leading-edge separation bubble causes an increase in nose-up moment, the moment changes to the nose-down direction as the size of the separation bubble increases. The effect of Reynolds number on $C_{m,0.25c}$ is similar to that of the lift slope (i.e., $C_{m,0.25c}$ changes to negative at a higher angle of attack at $Re \leq 2 \times 10^3$).

3.1.2. 3% thin circular arc airfoil

Figure 5 shows the aerodynamic characteristics of the 3% thin circular arc airfoil obtained varying the Reynolds number between 1×10^3 and 10×10^3. The nonlinearity of the lift curve is more remarkable than that of the flat plate. At

Fig. 5.   Aerodynamic characteristics of the 3% circular arc airfoil.

Fig. 6.   Aerodynamic characteristics of the 12% circular arc airfoil.
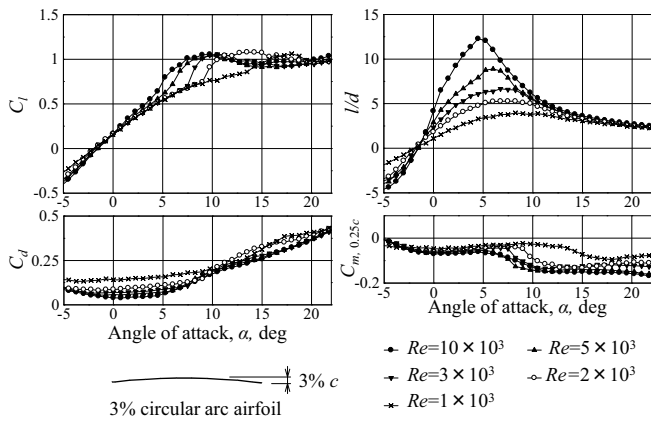

Fig. 7.   Aerodynamic characteristics of the 21% circular arc airfoil.

$Re = 10 \times 10^3$, the lift slope is small at $0 \deg < \alpha < 4 \deg$ and is large at $\alpha > 4 \deg$. The angle of attack at which the lift slope changes increases as the Reynolds number decreases. When the separated flow of the leading-edge separation bubble reattaches at the back of an apex on the upper surface, C_l increases significantly due to the large negative pressure generated by the leading-edge vortex. The lift slope then gradually decreases as the angle of attack increases, and C_l reaches the maximum. The discontinuous lift curves were observed for the low-camber airfoils at every Reynolds number.

The drag coefficient C_d increases as C_l increases, but the rate of the increase in C_d increases after the lift slope increases. The maximum lift-to-drag ratio $(l/d)_{\max}$, which is the largest in the Reynolds number range of this measurement, is obtained near the angle of attack corresponding to the rapid increase in lift slope.

The pitching moment coefficient $C_{m, 0.25c}$ shows a negative value at the zero-lift angle due to the effect of the positive camber, and $C_{m, 0.25c}$ has a slightly positive slope until the angle of attack where the lift slope increases largely. As the angle of attack largely increases, $C_{m, 0.25c}$ decreases to a large negative value because of the separation flow on the upper surface of the airfoil. The flow is easy to separate at a low Reynolds number. The corresponding smoke-flow is seen in the large-camber airfoil shown in Fig. 13, which is described later.

3.1.3.   12% thin circular arc airfoil

Figure 6 shows the aerodynamic characteristics of the 12% thin circular arc airfoil. As shown in the lift curve, a distinctive lift curve, which is the sudden increase and decrease in C_l at certain angles of attack caused by the leading-edge separation bubble, is specifically observed at $Re \geq 5 \times 10^3$. This phenomenon also occurs at a large Reynolds number as described by Mueller.[23] The lift curves of large-camber airfoils have rather continuous curves at $Re \leq 3 \times 10^3$ when compared to airfoils with smaller cambers.

The rate of increase in C_d becomes small at the angle of attack corresponding to the sudden increase in lift. At that time, $(l/d)_{\max}$ of $Re = 10 \times 10^3$ is obtained. As the Reynolds number decreases, $(l/d)_{\max}$ is obtained at the lower an-
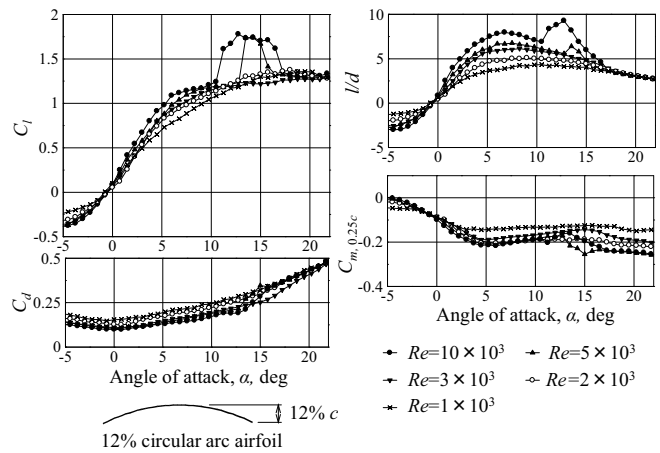
gle of attack.
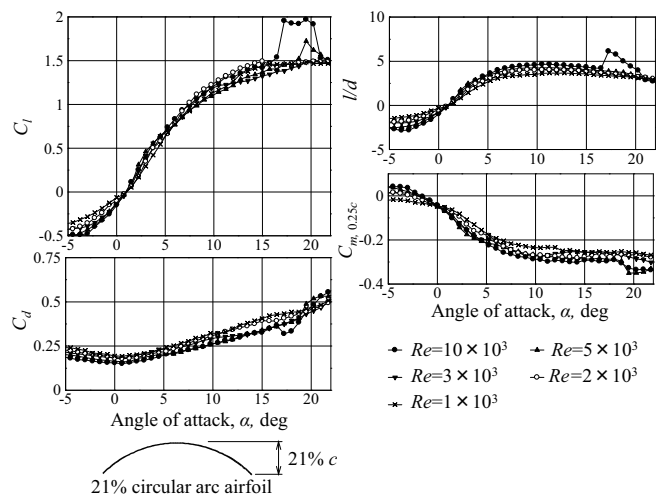
The pitching moment curve has a negative slope at $\alpha = 0 \deg$, and a small positive slope at $\alpha \geq 5 \deg$. The negative value of $C_{m, 0.25c}$ is large because of the effect of a large camber. When the lift increases suddenly, $C_{m, 0.25c}$ increases slightly once because of the nose-up moment caused by the negative pressure of the leading-edge separation bubble, and $C_{m, 0.25c}$ decreases as the angle of attack increases.

3.1.4.   21% thin circular arc airfoil

Figure 7 shows the aerodynamic characteristics of the 21% thin circular arc airfoil. The sudden increase in C_l at $Re \geq 5 \times 10^3$ is seen in the lift curve, and the corresponding angles of attack are large compared to those of the 12% camber airfoil. However, continuous lift curves are observed at $Re \leq 3 \times 10^3$. Although C_l is negative at $\alpha = 0 \deg$, a very large C_l of approximately 1.5 is obtained, even at $Re \leq 3 \times 10^3$.

The C_d and l/d curves are similar at various Reynolds numbers except for the case of the sudden increase in C_l at $Re = 10 \times 10^3$. The negative values of $C_{m, 0.25c}$ are large compared to those of the 12% camber airfoil at $\alpha \geq 5 \deg$. The continuous moment curves are observed like the contin-
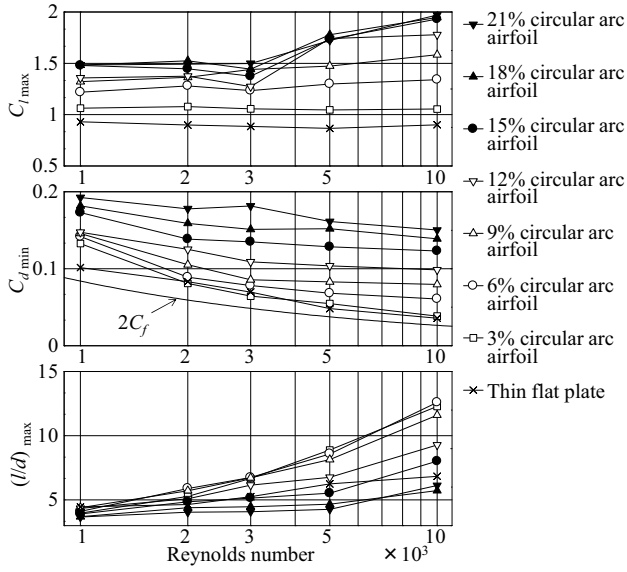
Fig. 8. Main aerodynamic characteristics of airfoils.

Fig. 9. Aerodynamic forces and moment on the airfoil coordinate system.

uous lift curve at $Re \leq 3 \times 10^3$.

It is important to note that the dependence of the aerodynamic characteristics of the 21% thin circular arc airfoil on the Reynolds number is negligible compared to that of the smaller camber airfoil at $Re \leq 3 \times 10^3$.

3.2. The main aerodynamic characteristics of circular arc airfoils

Figure 8 show the main aerodynamic characteristics of all the airfoils tested in this study: maximum lift coefficient $C_{l\max}$, minimum drag coefficient $C_{d\min}$ and maximum lift-to-drag ratio $(l/d)_{\max}$. Here, $C_{l\max}$ is considered in the measurement range of angles of attack. The error of measurement for $C_{d\min}$ estimated by the accuracy of the load cell was within 0.006, and that of $(l/d)_{\max}$ was within 0.2.

A higher $C_{l\max}$ is obtained for the thin circular arc airfoil with a larger camber at every Reynolds number. In particular, $C_{l\max}$ over 1.9 is obtained for the airfoils having cambers of $h \geq 15\%c$ as the Reynolds number increases to 10×10^3. These results are because of the sudden increase in lift seen in the lift curve caused by the leading-edge separation bubble, as stated later. As the Reynolds number decreases below 3×10^3, $C_{l\max}$ for the airfoils of $h \geq 15\%c$ is approximately 1.5, which is twice as large as that of the thin flat plate, and $C_{l\max}$ does not increase as camber increases. The changes in $C_{l\max}$ with the Reynolds number are small except that for the large-camber airfoils at $Re \geq 5 \times 10^3$.

The minimum drag coefficient $C_{d\min}$ is larger than twice the theoretical laminar skin friction drag $2C_f$ known as the Blasius friction law at every Reynolds number. $C_{d\min}$ of the 3% thin circular airfoil is similar to that of the thin flat plate having a thickness of 1.7%c at $Re \geq 2 \times 10^3$. $C_{d\min}$ of the thin circular airfoil increases as the camber increases at every Reynolds number.

The largest $(l/d)_{\max}$ is obtained by 3% and 6% thin circular arc airfoils at $Re = 10 \times 10^3$. It is approximately twice as large as those of 18% and 21% circular arc airfoils. As the Reynolds number decreases, the difference in $(l/d)_{\max}$ in air-
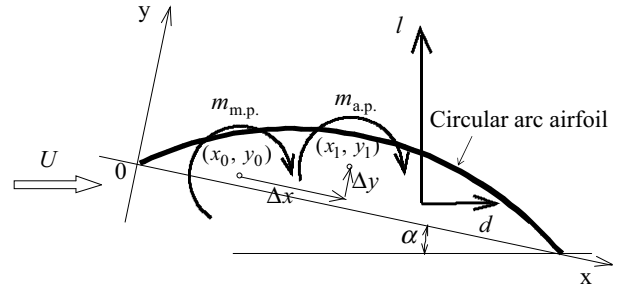
foils with various cambers decreases, and $(l/d)_{\max}$ is approximately 4 for all airfoils at $Re = 1 \times 10^3$. Therefore, it was found that $(l/d)_{\max}$ for thin circular arc airfoils having a very large camber is not smaller than the airfoils with smaller cambers at $Re = 1 \times 10^3$, and a high $C_{l\max}$ was obtained for the airfoil having a very large camber.

3.3. Consideration of the aerodynamic center

The aerodynamic center is defined as the location where the magnitude of the pitching moment remains constant with the change in the angle of attack. The theoretical aerodynamic center is generally close to the position of 1/4 chord. The pitching moment coefficient about 1/4 chord $C_{m,0.25c}$ at the zero-lift angle is negative for positive cambered airfoils, and is constant for all angle of attack below the stall angle. Since the pitching moment is the product of a force acting on the center of pressure and a moment arm that is the distance between the aerodynamic center and the center of pressure, the center of pressure moves on the chord as lift changes. As $C_{m,0.25c}$ is zero for a symmetric airfoil, the center of pressure is located at the aerodynamic center and is independent of the angle of attack. These well-known theoretical relations for a thin airfoil are effective under high Reynolds number conditions.

However, the aerodynamic center of an airfoil at a very-low Reynolds number is unknown, specifically in the case of large-camber airfoils, whose pitching moment has a negative slope at the zero-lift angle, as shown in Figs. 6 and 7. Further, the drag combined with the lift in force acting on the center of pressure is large at very-low Reynolds numbers. If the moment center is located at an appropriate position below the airfoil, this large drag may produce a positive moment that will oppose the negative moment due to the positive camber of the airfoil.

By defining the two centers of the moments on the coordinate axes of the airfoil as shown in Fig. 9, the pitching moment $m_{a.p.}$ about an arbitrary point (x_1, y_1) can be shifted from the moment $m_{m.p.}$ about the measurement point (x_0, y_0) using the following equation:

$$m_{a.p.} = m_{m.p.} + \left(\Delta x \cos \alpha + \Delta y \sin \alpha\right) l + \left(\Delta x \sin \alpha - \Delta y \cos \alpha\right) d \qquad (3)$$

Here,

$$\left. \begin{array}{l} \Delta x = x_1 - x_0 \\ \Delta y = y_1 - y_0 \end{array} \right\} \qquad (4)$$

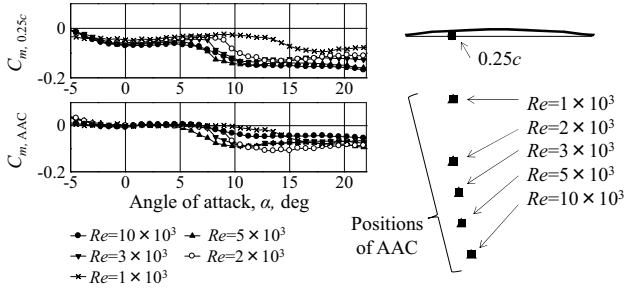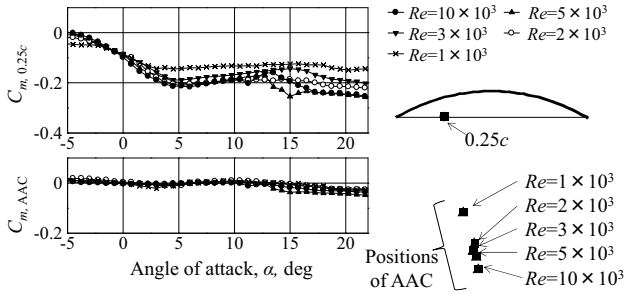Fig. 10. Pitching moment about AAC of the 3% circular arc airfoil.

Fig. 12. Pitching moment about AAC of the 21% circular arc airfoil.

Fig. 11. Pitching moment about AAC of the 12% circular arc airfoil.

Fig. 13. Flow visualization around the 21% thin circular airfoil.

The moment curve primarily undergoes a vertical shift along the y-axis with change in Δy, and rotates around the zero-lift angle with change in Δx. In our study, we shifted the point (x_1, y_1) so that the pitching moment about it was zero at a zero-lift angle, and kept it near zero even as the angle of attack increased. We refer to this point (x_1, y_1) as the alternative aerodynamic center (AAC) in this paper (i.e., $C_{m,\mathrm{AAC}} \cong 0$ and $\partial C_{m,\mathrm{AAC}}/\partial\alpha \cong 0$ in as wide a range of angles of attack as possible). Then, the point of AAC corresponds to the center of pressure when $C_{m,\mathrm{AAC}}$ is zero.

Figure 10 shows the comparison between $C_{m,0.25c}$ and $C_{m,\mathrm{AAC}}$ of the 3% thin circular arc airfoil obtained by setting the moment centers as illustrated in the figure. Because $C_{m,0.25c}$ is negative at $\alpha = 0$ deg, the AAC has to be located under the airfoil due to the generation of nose-up moment by the drag. Therefore, the distance between the AAC and airfoil increases as the Reynolds number increases because of the decrease in C_d. The $C_{m,\mathrm{AAC}}$ is zero at $\alpha < 5$ deg and $C_{m,\mathrm{AAC}}$ changes to negative at $\alpha \geq 5$ deg.

Figures 11 and 12 show $C_{m,\mathrm{AAC}}$ of the thin circular arc airfoils having cambers of $12\%c$ and $21\%c$, respectively. There were significant changes in the $C_{m,\mathrm{AAC}}$ of these airfoils, being different from those of smaller camber airfoils. The range of the angles of attack at $C_{m,\mathrm{AAC}} = 0$ increases as the camber increases; $C_{m,\mathrm{AAC}}$ is zero at $\alpha < 13$ deg for a 12% circular arc airfoil and at $\alpha < 18$ deg for a 21% circular arc airfoil at every Reynolds number. The position of the AAC has to be moved downward and backward from the point of 25% chord. In particular, the smaller distance of the AAC of the 21% circular arc airfoil was small at $Re = 1 \times 10^3$ because of the nose-up moment caused by large C_d.

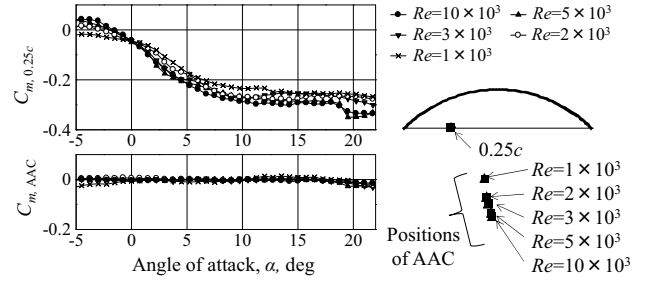From these results, it was found that the pitching moment
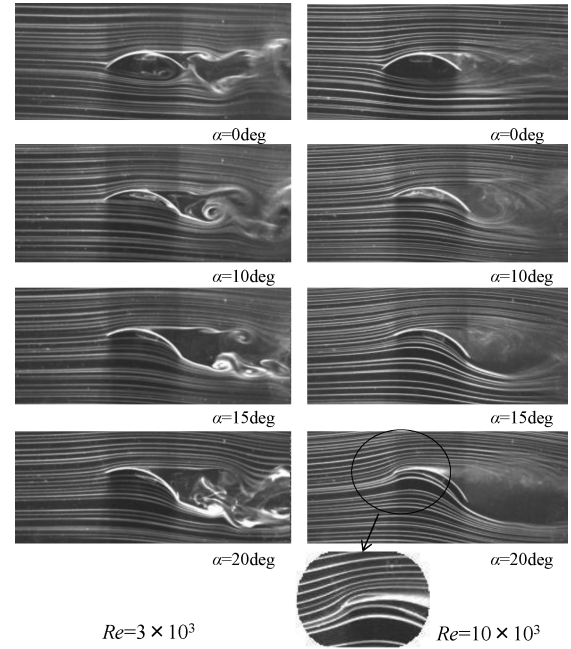
about the AAC of a large-camber circular arc airfoil was approximately zero over a wide range of angles of attack. The continuous decrease in $C_{m,0.25c}$ could be changed to the horizontal linear C_m curve by shifting the aerodynamic center. The location of AAC is the center of pressure when the pitching moment about AAC is zero. Therefore, it can be said that the center of pressure of a large-camber airfoil does not change in a wide range of angles of attack.

3.4. Flow visualization around the airfoil

Figure 13 shows the images of the streak lines around the 21% circular arc airfoil obtained using the smoke-wire method at $Re = 3 \times 10^3$ and 10×10^3. The flow of the upper surface separates at the highest point of the upper surface, and a large separation region is seen at the rear of the airfoil at each angle of attack. At $\alpha = 0$ deg, the streamline at the upstream of the leading-edge of the airfoil has a slightly downward direction, in which a negative lift acts on the airfoil, as seen in Fig. 8. The flow of the lower surface separates at the leading-edge and rolls up the vortices at the rear of the trailing-edge. At $\alpha = 10$ deg, the flow of the lower surface that separated at the leading-edge reattaches at the position of 80% chord (i.e., a leading-edge separation bubble

appears on the lower surface). The position of the reattachment moves forward as the angle of attack increases, and the separation flow of the lower surface disappears at $\alpha = 15$ deg. As the angle of attack increases, the separation bubble generated at the leading-edge is seen on the upper surface at 20 deg of $Re = 10 \times 10^3$, where the large C_l is seen in the lift curve of $Re = 10 \times 10^3$ in Fig. 8.

The continuous lift curves of $Re \le 3 \times 10^3$ in Fig. 8 are caused by the flow of the lower surface (i.e., the lift slope is large while the leading-edge separation bubble is seen on the lower surface, and the lift slope decreases as the separation range on the lower surface decreases). In contrast, the flow on the upper surface mostly does not change with changes in the angle of attack. Therefore, the lift slope decreases slowly as the reattachment point of the separation bubble moves forward.

It is important to note that the flow around the thin circular arc airfoil having a camber of 21%c did not change with changes in the Reynolds number, except at high angles of attack over 18 deg with Reynolds numbers higher than 5×10^3.

3.5. The pressure distribution of thin circular arc airfoil with a camber of 21%c

Figure 14 shows the distributions of the pressure coefficient C_p of the 21% circular arc airfoil at $Re = 5 \times 10^3$. At $-3 \deg \le \alpha \le 0 \deg$, positive C_p of the upper surface near the leading-edge decreases to the highest position where the C_p is negative, and it is almost constant without increasing toward the trailing-edge. As the angle of attack increases, C_p decreases mainly in the front part of the airfoil. The negative C_p of the lower surface is almost constant up to the 80% chord and increases toward the trailing-edge at $\alpha = -3$ deg. This pressure distribution shows that the leading-edge separation expands to the lower surface. In comparison to the flow visualizations (Fig. 13), the recovery range of the pres-
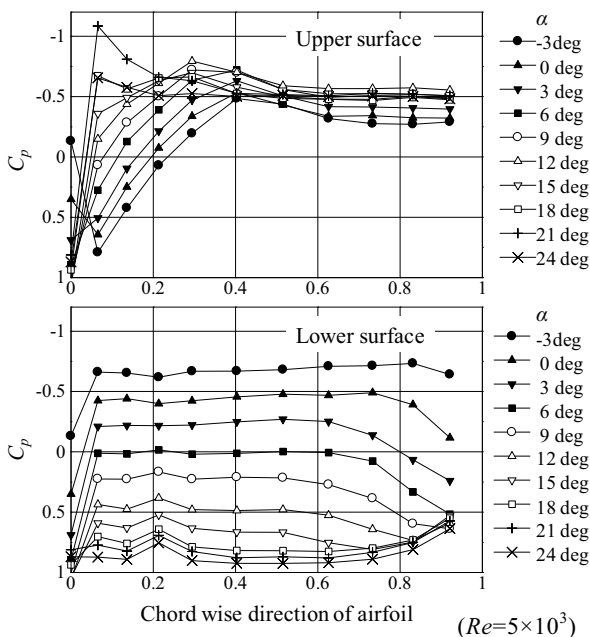
sure at the rear part of the airfoil increases as the reattachment point of the separation bubble moves forward. When separation at the lower surface disappears, the increase in pressure becomes small and the positive pressure increases at every point in the chord. These pressure changes cause the lift slope to slowly decrease, as shown in Fig. 7. As C_p of the upper surface near the leading-edge decreases at $18 \deg \le \alpha \le 24 \deg$, at which time the leading-edge separation bubble appears on the leading-edge of the wing, lift increases slightly.

In order to discuss the pitching moment obtained by integrating the product of the pressure distribution and the distance to the application point of the pressure, the pressure is classified into two types: one acting along the upper surface and the other acting along the lower surface. These pressures are expressed by attaching the subscripts "upper" and "lower", respectively. As shown in Fig. 15, the pressure $p_{\text{upper}}(x)$ that acts on the upper surface vertically as a function of x can be divided into its components along the x and y directions as:

$$\left.\begin{array}{l} p_{\text{x, upper}}(x) = p_{\text{upper}}(x) \sin \phi \\ p_{\text{y, upper}}(x) = p_{\text{upper}}(x) \cos \phi \end{array}\right\} \tag{5}$$

Similarly, $p_{\text{lower}}(x)$ on the lower surface is divided as:

$$\left.\begin{array}{l} p_{\text{x, lower}}(x) = p_{\text{lower}}(x) \sin \phi \\ p_{\text{y, lower}}(x) = p_{\text{lower}}(x) \cos \phi \end{array}\right\} \tag{6}$$

where ϕ is the tangent angle of the thin airfoil curve expressed by $y = f(x)$ and $\tan \phi$ is given by:

$$\tan \phi = \frac{\mathrm{d}y}{\mathrm{d}x} = f'(x) \tag{7}$$

The forces F_x and F_y, which are the components of the total force F along the x and y directions, respectively, are obtained by integrating the pressure components over the airfoil along the respective axis. This is shown in the following equation:

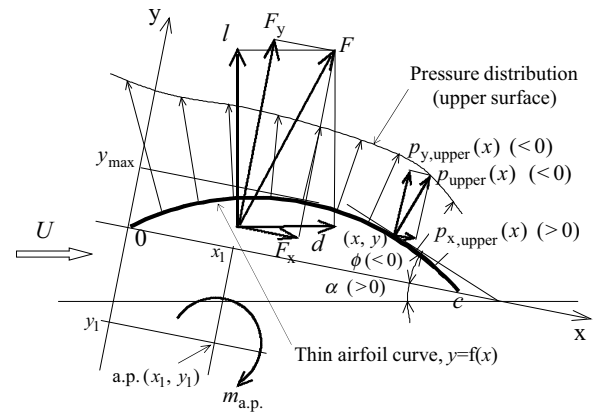Fig. 14. Pressure distributions of the 21% circular arc airfoil.

Fig. 15. Pressure components of x and y directions on the airfoil coordinate system.
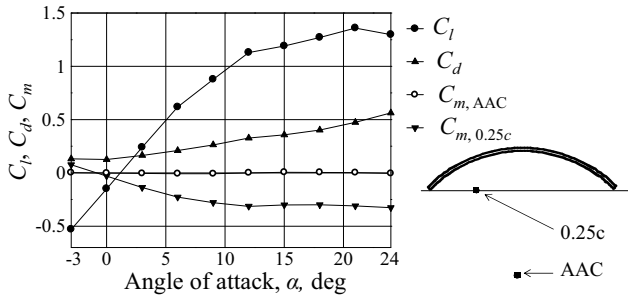
Fig. 16. Aerodynamic coefficients of the 21% circular arc airfoil obtained by integrating the pressure distributions.

Fig. 17. The C_d and $C_{m,\text{AAC}}$ obtained by considering the friction drag.

$$F_x = \int_0^c \left(-p_{x,\text{upper}}(x) + p_{x,\text{lower}}(x) \right) \tan\phi \, dx \quad \left.\right\}$$
$$F_y = \int_0^c \left(-p_{y,\text{upper}}(x) + p_{y,\text{lower}}(x) \right) dx \quad (8)$$

Then, the lift l and drag d are obtained as:

$$\begin{bmatrix} l \\ d \end{bmatrix} = \begin{bmatrix} \cos\alpha & -\sin\alpha \\ \sin\alpha & \cos\alpha \end{bmatrix} \begin{bmatrix} F_y \\ F_x \end{bmatrix} \quad (9)$$

The pitching moment $m_{\text{a.p.}}$ about the arbitrary point (x_1, y_1) is obtained by the following equation:

$$m_{\text{a.p.}} = \int_0^c \Big\{ \left(f(x) - y_1 \right) \left(p_{x,\text{upper}}(x) - p_{x,\text{lower}}(x) \right) \\ - (x - x_1) \left(p_{y,\text{upper}}(x) - p_{y,\text{lower}}(x) \right) \Big\} \, dx \quad (10)$$

Figure 16 shows the aerodynamic coefficients obtained by integrating the pressure distributions. In this case, the suction force acting forward on the leading-edge was negligible due to the small area of pressure surface on the thin airfoil. Although the lift and drag coefficients (C_l, C_d) show curves similar to that of the force measured, the maximum lift coefficient $C_{l\max}$ is smaller than that of the force measured. The reason seems to be the thickness of the wing model used for the pressure measurement being slightly large owing to the structure of the wing model having pressure holes.

The pitching moment coefficient $C_{m,0.25c}$ corresponds to the moment measured directly. The $C_{m,\text{AAC}}$ is approximately zero at every angle of attack by setting the AAC at the low position under the airfoil. The location of the AAC is near the geometrical center of the circular arc airfoil as shown in Fig. 16. This is because the pressure applied vertically on the circular arc surface does not generate moment around the geometrical center. Although the AAC obtained in Fig. 12 was close to the position obtained by the pressure distribution method, there was a positional difference due to the Reynolds number. The cause of this difference is the skin friction drag, which is not contained in the pressure drag coefficient C_{dp} obtained by integrating the pressure distribution. By considering double the laminar skin friction drag coefficient $2C_f$, where C_f is given by $C_f = 1.328/\sqrt{Re}$ (i.e., the Blasius friction law), C_d is expressed as $C_d = C_{dp} + 2C_f$. This is a rough estimation because the friction
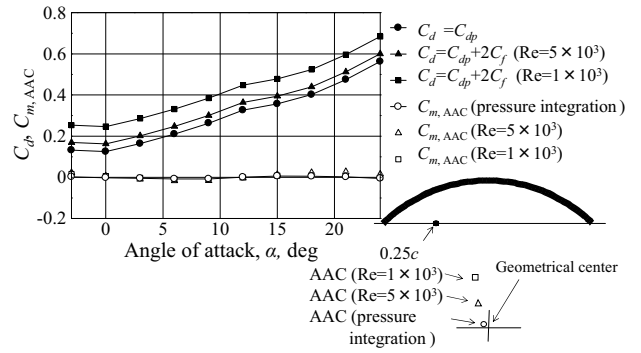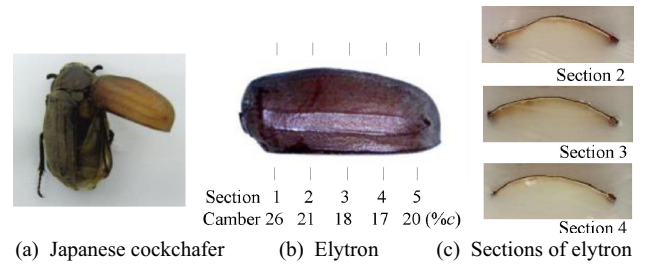
drag will change with not only the Reynolds number, but also the angle of attack due to the attached flow and separated flow over the wing. The C_d and $C_{m,\text{AAC}}$ obtained by considering the friction drag of each Reynolds number are shown in Fig. 17. When C_d increased with the addition of $2C_f$, the location of AAC moved forward as the Reynolds number decreased. The locations of AAC were very close to those illustrated in Fig. 12.

Thus, the effect of friction drag was large for $C_{m,\text{AAC}}$. Further, the friction drag was constant regardless of the angle of attack because $C_{m,\text{AAC}}$ showed a constant value of nearly zero, as shown in Fig. 17. This seems to be caused by the friction drag, which does not change in the thin circular arc airfoil with a large camber at the time of the large separation flow on the upper surface, where flow speed is larger than that on the lower surface. The unchanged $C_{m,\text{AAC}}$ of the large-camber airfoil is considered to be the result of the circular arc shape and the large friction drag at very-low Reynolds numbers.

3.6. Aerodynamic characteristics of the three-dimensional wing of elytra

Figure 18(a) shows the elytron of the Japanese cockchafer, used in this experiment. When the insect flies, the Reynolds number of the elytron is 3×10^3 or less.[17] The elytron has thin sections with large cambers, as shown in Figs. 18(b) and (c). The three-dimensional wing model used for the wind tunnel tests is a pair of the elytron of the Japanese cockchafer (i.e., elytra are coupled at the elytron root by a thin flat plate). The wing model was supported by a piano wire rod 0.8 mm in diameter, as shown in Fig. 19.

Figure 20 shows the aerodynamic characteristics of the elytron obtained at $Re = 2 \times 10^3$–3×10^3 and the thin alu-

(a) Japanese cockchafer (b) Elytron (c) Sections of elytron

Fig. 18. Elytron of Japanese cockchafer.
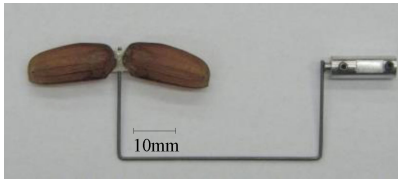
Mean aerodynamic chord
$\bar{c} = 7.72\,\mathrm{mm}$

Wing width $b = 40.6\,\mathrm{mm}$

Wing area $S = 302\,\mathrm{mm}^2$

Aspect ratio $AR = 5.45$

Fig. 19. Wing model for the wind tunnel tests.

Elytra
$Re = 3 \times 10^3$
$Re = 2 \times 10^3$

Thin flat plate
$Re = 2 \times 10^3$

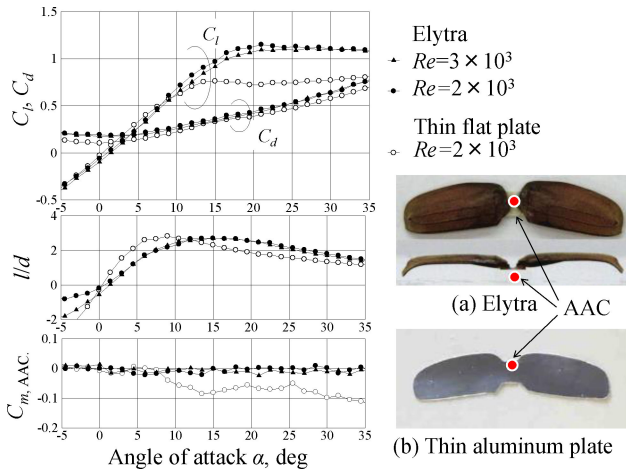(a) Elytra — AAC

(b) Thin aluminum plate

Fig. 20. Aerodynamic characteristics of the elytra.

minum flat plate having a thickness of 0.2 mm and the same profile at $Re = 2 \times 10^3$, which are included for comparison. The maximum angle of attack considered for this experiment is large because the lift slope was smaller than that of the above experiments due to the three-dimensional wing. However, the blockage effect of this test is small due to the small chord length. As shown in Fig. 20, the lift coefficient C_l increases as the angle of attack increases, and $C_{l\max}$ is larger than that of the flat plate. The drag coefficient C_d was large compared to that of the flat plate. However, $(l/d)_{\max}$, which is similar to that of the flat plate, was obtained at a larger angle of attack than that of the flat plate. The moment coefficient was expressed by setting the modified aerodynamic center to the point illustrated in Fig. 20. The $C_{m,\mathrm{AAC}}$ of the elytra shows a constant value of approximately zero over a wide range of angles of attack compared to that of the flat plate. That is, the center of pressure, which corresponds to the AAC, does not move as the angle of attack changes.

Although the wing having a pitching moment of zero does not stabilize itself, it is easy to set the body at various angles of attack in flight when it has the tail or other wings to change the angle of attack. This will mean that a micro-air vehicle having large-camber wings will be able to effectively stabilize the vehicle at various angles of attack by locating the center of gravity on the AAC, because the center of pressure of the wing does not move when the angle of attack changes. The beetle actually has its body under the elytra and has the hind wings, which generate the lift and thrust at the lower rear of the elytra.

4. Conclusion

To obtain the aerodynamic characteristics of a large-camber thin circular arc airfoil by comparing airfoils having cambers varying from 3%c to 21%c, low-pressure wind tunnel tests were conducted at Reynolds number ranging between 1×10^3 and 10×10^3, and the following results were obtained:

1) The discontinuous lift curves of circular arc airfoils having small camber and a thin flat plate are significant as the Reynolds number decreases.

2) A sudden increase in lift is observed in the lift curves of thin circular arc airfoils having a camber over 12%c at $Re \geq 5 \times 10^3$. At $Re \leq 3 \times 10^3$, this phenomenon does not occur and continuous lift curves are obtained for the airfoil having a camber of 21%c.

3) The lift coefficient C_l for the airfoils having a camber over 15%c reaches 1.5 at $Re \leq 3 \times 10^3$.

4) As the Reynolds number decreases, the difference in the maximum lift-to-drag ratio $(l/d)_{\max}$ becomes small, which is not seen at $Re = 1 \times 10^3$.

5) The pitching moment coefficient $C_{m,0.25c}$ for the 21% circular arc airfoil has a negative slope at $\alpha = 0\,\mathrm{deg}$, and shows a large negative constant value at $\alpha > 10\,\mathrm{deg}$.

6) The pitching moment coefficient for the 21% circular arc airfoil is approximately zero over a wide range of angles of attack by adjusting the position of the moment center. The location of this moment center, which is referred as AAC in this paper, is located behind and beneath the position of 25% chord. Therefore, the center of pressure located on the AAC of a large-camber airfoil does not move in a wide range of angles of attack.

7) For a large-camber airfoil, the pitching moment coefficient around the AAC ($C_{m,\mathrm{AAC}}$) of zero is due to the circular arc shape and the large friction drag at very-low Reynolds numbers.

8) $C_{m,\mathrm{AAC}}$ for a small wing such as elytra having a large-camber thin circular arc airfoil is zero over a wide range of angles of attack.

References

1) Okamoto, M., Yasuda, K., and Azuma, A.: Aerodynamic Characteristics of the Wings and Body of a Dragonfly, *J. Exp. Biol.*, **199** (1996), pp. 281–294.
2) Azuma, A., Okamoto, M., and Yasuda, K.: Aerodynamic Characteristics of Wing at Low Reynolds Number, Mueller, T. J., ed., *Fixed and Flapping Wing Aerodynamics for Micro Air Vehicle Applications*, Progress in Astronautics and Aeronautics, Vol. 195, AIAA, 2001, pp. 341–398.

3) Kesel, A. B.: Aerodynamic Characteristics of Dragonfly Wing Sections Compared with Technical Aerofoils, *J. Exp. Biol*, **203** (2000), pp. 2125–2135.

4) Sunada, S., Yasuda, T., Yasuda, K., and Kawachi, K.: Comparison of Wing Characteristics at an Ultralow Reynolds Number, *J. Aircraft*, **39**, 2 (2002), pp. 331–338.

5) Zhou, Y., Alam, M. M., Yang, H. X., Guo, H., and Wood, D. H.: Fluid Forces on a Very Low Reynolds Number Airfoil and Their Prediction, *Int. J. Heat Fluid Flow*, **32**, 1 (2011), pp. 329–339.

6) Okamoto, M. and Azuma, A.: Aerodynamic Characteristics at Low Reynolds Numbers for Wings of Various Planforms, *AIAA J.*, **49**, 6 (2011), pp. 1135–1150.

7) Obata, A. and Shinohara, S.: Flow Visualization Study of the Aerodynamics of Modeled Dragonfly Wings, *AIAA J.*, **47**, 12 (2009), pp. 3043–3047.

8) Shi, S. X., Liu, Y. Z., and Chen, J. M.: An Experimental Study of Flow around a Bio-inspired Airfoil at Reynolds Number 2.0×10^3, *J. Hydrodynamics*, **24**, 3 (2012), pp. 410–419.

9) Kunz, P. and Kroo, I.: Airfoil Analysis and Design, Mueller, T. J., ed., *Fixed and Flapping Wing Aerodynamics for Micro Air Vehicle Applications*, Progress in Astronautics and Aeronautics, Vol. 195, AIAA, 2001, pp. 35–60.

10) Vargas, A., Mittal, R., and Dong, H.: A Computational Study of the Aerodynamic Performance of a Dragonfly Wing Section in Gliding Flight, *Bioinsp. Biomim.*, **3** (2008), pp. 1–13.

11) Levy, D. E. and Seifert, A.: Parameter Study of Simplified Dragonfly Airfoil Geometry at Reynolds Number of 6000, *J. Theor. Biol.*, **266**, 4 (2010), pp. 691–702.

12) Kim, W., Ko, J., Park, H., and Byun, D.: Effects of Corrugation of the Dragonfly Wing on Gliding Performance, *J. Theor. Biol*, **260**, 4 (2009), pp. 523–530.

13) Hord, K. and Lian, Y.: Numerical Investigation of the Aerodynamic and Structural Characteristics of a Corrugated Airfoil, *J. Aircraft*, **49**, 3 (2012), pp. 749–757.

14) Hidaka, H. and Okamoto, M.: An Experimental Study of Triangular Airfoil for Mars Airplane, *Trans. JSASS Aerospace Technology Japan*, **12**, ists 29 (2014), pp. Pk_21–Pk_27.

15) Sitorusa, P. E., Park, H. C., Byun, D., Goo, N. S., and Han, C. H.: The Role of Elytra in Beetle Flight: I. Generation of Quasi-Static Aerodynamic Forces, *J. Bionic Eng.*, **7**, 4 (2010), pp. 354–363.

16) Le, T. Q., Truong, T. V., Tran, H. T., Park, S. H., Ko, J. H., Park, H. C., and Byun, D.: How Could Beetle's Elytra Support Their Own Weight during Forward Flight? *J. Bionic Eng.*, **11**, 4 (2014), pp. 529–540.

17) Okamoto, M. and Ebina, K.: Aerodynamic Characteristics of Elytra of Beetles, 32th Aero Aqua Bio-mechanisms Symposium, 2015, Japan, pp. 31–32 (in Japanese).

18) Anyoji, M., Okamoto, M., Hidaka, H., Nonomura, T., Oyama, A., and Fujii, K.: Planetary Atmosphere Wind Tunnel Tests on Aerodynamic Characteristics of a Mars Airplane Scale Model, *Trans. JSASS Aerospace Technology Japan*, **12**, ists 29 (2014), pp. Pk_7–Pk_12.

19) Anyoji, M., Nose, K., Ida, S., Numata, D., Nagai, H., and Asai, K.: Low Reynolds Number Airfoil Testing in a Mars Wind Tunnel, 40th Fluid Dynamics Conference and Exhibit, Chicago, Illinois, AIAA 2010-4627, 2010.

20) Wood, R. J., Finio, B., Karpelson, M., Ma, K., Perez-Arancibia, N. O., Sreetharan, P. S., Tanaka, H., and Whitney, J. P.: Progress on Pico Air Vehicles, *Int. J. Robot. Res.*, **31**, 11 (2012), pp. 1292–1302.

21) Kroo, I. and Kunz, P.: Mesoscale Flight and Miniature Rotorcraft Development, Mueller, T. J., ed., *Fixed and Flapping Wing Aerodynamics for Micro Air Vehicle Applications*, Progress in Astronautics and Aeronautics, Vol. 195, AIAA, 2001, pp. 503–517.

22) Roshko, A.: Experiments on the Flow Past a Circular Cylinder at Very High Reynolds Numbers, *J. Fluid Mec.*, **10** (1960), pp. 345–356.

23) Mueller, T. J.: Aerodynamic Measurements at Low Reynolds Numbers for Fixed Wing Micro-Air Vehicles, Presented at the RTO AVT/VKI Special Course on Development and Operation of UAVs for Military and Civil Applications, 1999.

24) Crompton, M. J. and Barrett, R. V.: Investigation of the Separation Bubble Formed behind the Sharp Leading Edge of a Flat Plate at Incidence, *Proc. Inst. Mech. Eng.*, **214** (2000), pp. 157–176.

J. Cho
Associate Editor